IEICE TRANSACTIONS

on Electronics

VOL. E106-C NO. 7
JULY 2023

A PUBLICATION OF THE ELECTRONICS SOCIETY

The Institute of Electronics, Information and Communication Engineers
Kikai-Shinko-Kaikan Bldg., 5-8, Shibakoen 3chome, Minato-ku, TOKYO, 105-0011 JAPAN

BRIEF PAPER

Contrast Source Inversion for Objects Buried into Multi-Layered Media for Subsurface Imaging Applications

Yoshihiro YAMAUCHI[†], ***Nonmember and*** **Shouhei KIDERA**[†a)], ***Senior Member***

SUMMARY This study proposes a low-complexity permittivity estimation for ground penetrating radar applications based on a contrast source inversion (CSI) approach, assuming multilayered ground media. The homogeneity assumption for each background layer is used to address the ill-posed condition while maintaining accuracy for permittivity reconstruction, significantly reducing the number of unknowns. Using an appropriate initial guess for each layer, the post-CSI approach also provides the dielectric profile of a buried object. The finite difference time domain numerical tests show that the proposed approach significantly enhances reconstruction accuracy for buried objects compared with the traditional CSI approach.
key words: *ground penetrating radar (GPR), multi-layer ground model, inverse scattering problem, contrast source inversion (CSI)*

1. Introduction

Owing to its effectiveness in preventing catastrophic road or tunnel collapses caused by aging or earthquake, the demand for nondestructive testing of infrastructure, such as roads or objects buried in the ground, has grown in recent years. Although electromagnetic testing techniques, such as electric inspection [1], [2] or bore hole radar [3], are promising, the requirement of driving electrodes into the ground makes them unsuitable for speedy and cost-saving screening. As a promising alternative, microwave ground penetrating radar (GPR) has some advantages, such as quick investigation with compact equipment, which also provides a deep penetration depth for low loss media, such as dry sand or soil, and high range resolution using an ultra wideband signal. The major approach for GPR imaging issues is the confocal approach, such as a synthetic aperture process [4] or range migration approach [2], which enhances cross-range resolution using an equivalently large aperture. However, the above radar approach rarely retrieves an object's dielectric property, and the image reconstruction accuracy is highly dependent on the background propagation model, which is usually assumed to be homogeneous media with known relative permittivity. Although several studies have focused on multiple layered backgrounds [5], they are based on some unrealistic assumptions, such as complete knowledge of relative permittivity for each layer, and in particular, suffer from unnecessary responses caused by multiple reflections among layers.

In contrast, inverse scattering approaches have been considered in recent years for the GPR model, where it provides a quantitative profile of the complex permittivity of an object by solving the domain integral equation. In general, the above inverse scattering problem has a nonlinear property, and the ill-posed condition becomes severe in the GPR model because a limited angle of measurement is available. Although some studies have focused on the inverse scattering approach [3], [6], they still suffer from inaccuracy due to the above ill-posed condition, especially for local optimization problems with inappropriate initial estimates.

Focusing on the permittivity estimation for ground media, the common middle point scheme is one of the most major approaches [7], however, it is not basically applicable to mono-static or bi-static configuration with fixed separation, which limits the applicability range. We introduce a contrast source inversion (CSI) scheme, which is based on an initial estimate of the relative permittivity of a multilayer model, to address the aforementioned issue. CSI is a potential inverse scattering (IS) method with lower complexity that simultaneously solves the state and data equations, avoiding the iterative use of the forward solver, such as the finite difference time domain (FDTD) [8], [9]. Focusing on the CSI features, we introduce cost function minimization based on relative permittivity estimation using the assumption that each layer has a homogeneous media. This approach was initially developed by Morimoto [10], who assumed terahertz band imaging, but ignored buried object imaging, and only aimed at relative permittivity estimation for each layer. Different from the above study [10], we apply the post-CSI approach using the initial estimate of the relative permittivities of multilayers, part of which has been reported in [11]. The FDTD-based numerical tests, assuming a three-multilayer background with an air cavity object, demonstrate that the proposed method considerably enhances reconstruction accuracy compared with that obtained by the traditional CSI method.

2. Method

2.1 Observation Model

The observation model, assuming multi-layered subsurface imaging, is shown in Fig. 1, where a single set of transmitter and receiver is scanned on a straight line in parallel with the y axis. $E^{\mathrm{T}}(\omega; \boldsymbol{r}_{\mathrm{T}}, \boldsymbol{r}_{\mathrm{R}})$ denotes the total electric

Manuscript received August 8, 2022.
Manuscript revised October 14, 2022.
Manuscript publicized January 20, 2023.
[†]The authors are with Graduate School of Informatics and Engineering, University of Electro-Communications, Chofu-shi, 182–8585 Japan.
a) E-mail: kidera@uec.ac.jp
DOI: 10.1587/transele.2022ECS6008

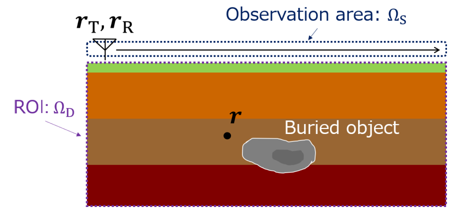

Fig. 1 Observation model.

field, recorded at $\boldsymbol{r}_{\mathrm{R}}$, where the transmitter is located at $\boldsymbol{r}_{\mathrm{T}}$. Ω_{S} and Ω_{D} defines an observation area and a region of interest (ROI), respectively. Each layer is assumed to have a uniform dielectric profile parallel to the scanning line, and the thickness of each layer is given, for simplicity. Here the scattered electric field is defined as: $E^{\mathrm{S}}(\omega; \boldsymbol{r}_{\mathrm{T}}, \boldsymbol{r}_{\mathrm{R}}) \equiv E^{\mathrm{T}}(\omega; \boldsymbol{r}_{\mathrm{T}}, \boldsymbol{r}_{\mathrm{R}}) - E^{\mathrm{I}}(\omega; \boldsymbol{r}_{\mathrm{T}}, \boldsymbol{r}_{\mathrm{R}})$, where ω is the angular frequency and $E^{\mathrm{I}}(\omega; \boldsymbol{r}_{\mathrm{T}}, \boldsymbol{r}_{\mathrm{R}})$ denotes the incident electric field.

2.2 Contrast Source Inversion

We introduce the CSI method as a promising inverse scattering approach in terms of lower complexity and accuracy. The methodology is briefly presented as follows. First, the scattered electric field $E^{\mathrm{S}}(\omega; \boldsymbol{r}_{\mathrm{T}}, \boldsymbol{r}_{\mathrm{R}})$, defined in the previous paragraph, is formulated by the following domain integral equation:

$$E^{\mathrm{S}}(\omega; \boldsymbol{r}_{\mathrm{T}}, \boldsymbol{r}') = k_{\mathrm{B}}^2 \int_{\Omega_{\mathrm{D}}} G_{\mathrm{B}}(\omega; \boldsymbol{r}, \boldsymbol{r}') w(\omega; \boldsymbol{r}_{\mathrm{T}}, \boldsymbol{r}) d\boldsymbol{r}, \quad (1)$$

Here k_{B} and $G_{\mathrm{B}}(\omega; \boldsymbol{r}, \boldsymbol{r}')$ express the wave number and the Green's function of the background media, respectively, which is defined as $\epsilon_{\mathrm{B}}(\boldsymbol{r})$. The contrast function is defined as $\chi(\omega; \boldsymbol{r}) \equiv (\epsilon(\omega; \boldsymbol{r}) - \epsilon_{\mathrm{B}}(\boldsymbol{r}))/\epsilon_{\mathrm{B}}(\boldsymbol{r})$ where $\epsilon(\omega; \boldsymbol{r})$ denotes the complex permittivity at the specific angular frequency ω at the position $\boldsymbol{r}$ including the object. As the dummy variable in the optimization process, the contrast source $w(\omega; \boldsymbol{r}_{\mathrm{T}}, \boldsymbol{r}) \equiv \chi(\omega; \boldsymbol{r}) E^{\mathrm{T}}(\omega; \boldsymbol{r}_{\mathrm{T}}, \boldsymbol{r})$ is introduced. CSI focuses on the two physical conditions that Eq. (1) must be satisfied at $\boldsymbol{r}' \in \Omega_{\mathrm{S}}$ and $\boldsymbol{r}' \in \Omega_{\mathrm{D}}$. In the original CSI scheme, $\chi(\omega; \boldsymbol{r})$ and $w(\omega; \boldsymbol{r}_{\mathrm{T}}, \boldsymbol{r})$ are simultaneously optimized using the following formula:

$$(\hat{\chi}(\boldsymbol{r}), \hat{w}) = \arg\min_{\chi, w} F(\chi, w) \quad (2)$$

$$F(\chi, w) \equiv \frac{\sum_{\boldsymbol{r}_{\mathrm{T}}} \|E^{\mathrm{S}}(\omega; \boldsymbol{r}_{\mathrm{T}}, \boldsymbol{r}_{\mathrm{R}}) - \mathcal{G}^{S}[w]\|_{\Omega_{\mathrm{S}}}^2}{\sum_{\boldsymbol{r}_{\mathrm{T}}} \|E^{\mathrm{S}}(\omega; \boldsymbol{r}_{\mathrm{T}}, \boldsymbol{r}_{\mathrm{R}})\|_{\Omega_{\mathrm{S}}}^2} + \frac{\sum_{\boldsymbol{r}_{\mathrm{T}}} \|\chi(\omega; \boldsymbol{r}) E^{\mathrm{I}}(\omega; \boldsymbol{r}_{\mathrm{T}}, \boldsymbol{r}') - w(\omega; \boldsymbol{r}_{\mathrm{T}}, \boldsymbol{r}') + \chi(\omega; \boldsymbol{r}') \mathcal{G}^{D}[w]\|_{\Omega_{\mathrm{D}}}^2}{\sum_{\boldsymbol{r}_{\mathrm{T}}} \|\chi(\omega; \boldsymbol{r}') E^{\mathrm{I}}(\omega; \boldsymbol{r}_{\mathrm{T}}, \boldsymbol{r}')\|_{\Omega_{\mathrm{D}}}^2}, \quad (3)$$

Here $\mathcal{G}^{\mathrm{S}}$ and $\mathcal{G}^{\mathrm{D}}$ are defined as follows:

$$\mathcal{G}^{\mathrm{S}}[w] = k_{\mathrm{B}}^2 \int_{\Omega_{\mathrm{D}}} G_{\mathrm{B}}(\omega; \boldsymbol{r}, \boldsymbol{r}_{\mathrm{R}}) w(\omega; \boldsymbol{r}_{\mathrm{T}}, \boldsymbol{r}) d\boldsymbol{r}, (\boldsymbol{r}_{\mathrm{R}} \in \Omega_{\mathrm{S}}), \quad (4)$$

$$\mathcal{G}^{\mathrm{D}}[w] = k_{\mathrm{B}}^2 \int_{\Omega_{\mathrm{D}}} G_{\mathrm{B}}(\omega; \boldsymbol{r}, \boldsymbol{r}') w(\omega; \boldsymbol{r}_{\mathrm{T}}, \boldsymbol{r}) d\boldsymbol{r}, (\boldsymbol{r}' \in \Omega_{\mathrm{D}}), \quad (5)$$

where $\|\cdot\|_{\Omega_{\mathrm{S}}}^2$ and $\|\cdot\|_{\Omega_{\mathrm{D}}}^2$ are the l_2 norms defined in Ω_{S} and Ω_{D}, respectively. Since the total field in the ROI $E^{\mathrm{T}}(\omega; \boldsymbol{r}_{\mathrm{T}}, \boldsymbol{r})$, included in $w(\omega; \boldsymbol{r}_{\mathrm{T}}, \boldsymbol{r})$, is simultaneously optimized, it does not require an iterative computation of the forward solver, such as the FDTD method, and then, it achieves significantly lower complexity, than other approaches, such as distorted Born iterative method (DBIM). However, if a larger scale of ROI is assumed, it suffers severely from the ill-posed condition, that the number of unknowns exceed than that of the measurement data.

2.3 Proposed Method

To overcome the above ill-posed condition problem, we introduce a scheme for massively reducing the number of unknowns by assuming that each background layer has homogeneous media with constant permittivity, which is usually acceptable in various GPR situations. A similar idea has been developed in the terahertz waveband analysis [10], however, the study did not focus on buried object imaging assuming ground penetrating applications.

2.3.1 Permittivity Estimation for Each Layer

Meanwhile, the proposed method focuses on the permittivity estimation of each layer as background media in the first step, excluding buried objects. Assuming the above condition, a variable for the permittivity for each layer is defined as $\boldsymbol{\epsilon}_{\mathrm{ML}} \equiv (\epsilon_1, \ldots, \epsilon_n, \ldots, \epsilon_{N_{\mathrm{layer}}})$, where ϵ_i denotes the permittivity of the i-th layer and the N_{layer} is the number of layers. Thus, the contrast function assuming the multi-layer model $\chi(\boldsymbol{r}; \boldsymbol{\epsilon}_{\mathrm{ML}})$ is then defined as follows:

$$\chi(\boldsymbol{r}; \boldsymbol{\epsilon}_{\mathrm{ML}}) \equiv \chi_i, \ (\boldsymbol{r} \in \Omega_{\mathrm{D},i}, \ i = 1, \ldots, N_{\mathrm{layer}}) \quad (6)$$

where $\Omega_{\mathrm{D},i}$ denotes the i-th layer of the ROI. $\chi_i \equiv \left(\epsilon_i + \frac{\sigma_i}{j\omega\epsilon_0} - \epsilon_{\mathrm{B,vc}}\right)/\epsilon_{\mathrm{B,vc}}$, where σ_i is the conductivity of the i-th layer. Note that, for simplicity, this study assumes that σ_i is given.

To determine the optimal solution of $\boldsymbol{\epsilon}_{\mathrm{ML}}$, the cost function in Eq. (3) for assuming $\chi(\boldsymbol{r}; \boldsymbol{\epsilon}_{\mathrm{ML}})$, is minimized in terms of the variable $w(\omega, \boldsymbol{r}_{\mathrm{T}}, \boldsymbol{r})$, using the CSI updating sequences, where the $\epsilon_{\mathrm{B,vc}} = 1$, namely, the vacuum background. The minimized residual for the assumed multi-layer variable $\chi(\boldsymbol{r}; \boldsymbol{\epsilon}_{\mathrm{ML}})$ is calculated as follows:

$$\tilde{F}(\boldsymbol{\epsilon}_{\mathrm{ML}}) = \min_{w} F(\chi(\boldsymbol{r}; \boldsymbol{\epsilon}_{\mathrm{ML}}), w) \quad (7)$$

Each permittivity for layer $\boldsymbol{\epsilon}_{\mathrm{ML}} \equiv (\hat{\epsilon}_1, \ldots, \hat{\epsilon}_n, \ldots, \hat{\epsilon}_{N_{\mathrm{layer}}})$ is determined as:

$$\hat{\boldsymbol{\epsilon}}_{\mathrm{ML}} = \arg\min_{\boldsymbol{\epsilon}_{\mathrm{ML}}} \tilde{F}(\boldsymbol{\epsilon}_{\mathrm{ML}}) \quad (8)$$

Then, the initial estimate for $\hat{\chi}(\boldsymbol{r}; \boldsymbol{\epsilon}_{\mathrm{ML}})$ is updated as:

$$\hat{\chi}(\boldsymbol{r}; \hat{\boldsymbol{\epsilon}}_{\mathrm{ML}}) \equiv \hat{\chi}_i, \ (\boldsymbol{r} \in \Omega_{\mathrm{D},i}, \ i = 1, \ldots, N_{\mathrm{layer}}) \quad (9)$$

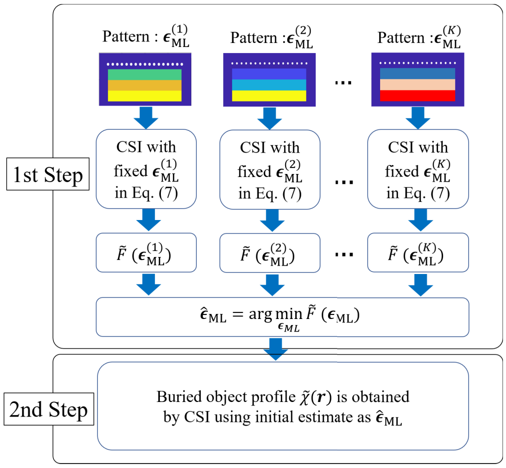

Fig. 2 Flowchart of the proposed scheme.

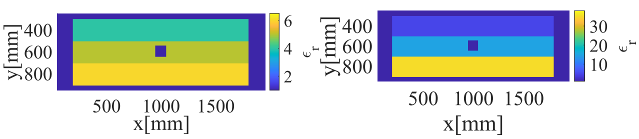

(a) Case #1 (b) Case #2

Fig. 3 Ground truth profiles of relative permittivity.

where $\hat{\chi}_i \equiv \left(\hat{\epsilon}_i + \frac{\sigma_i}{j\omega\epsilon_0} - \epsilon_{\mathrm{B,vc}}\right)/\epsilon_{\mathrm{B,vc}}$ holds. Figure 2 shows the processing flow of the proposed method. Note that, the processes in Eqs. (7)–(9) are performed in parallel for each combination of $\boldsymbol{\epsilon}_{\mathrm{ML}}$, as shown in Fig. 2. Particularly, the optimal solution of $\boldsymbol{\epsilon}_{\mathrm{ML}}$ is searched from all possible combinations of $\boldsymbol{\epsilon}_{\mathrm{ML}}$ to avoid a local optimal issue.

2.3.2 Object Reconstruction

At the second step, the CSI scheme with the updated initial estimate as $\hat{\chi}(\boldsymbol{r}; \hat{\boldsymbol{\epsilon}}_{\mathrm{ML}})$ is used to reconstruct a buried object. While this method neglects the existence of buried objects at the first stage, in determining the permittivity pattern in Eq. (8), a more appropriate initial estimate (*i.e.*, the multi-layer profile) could provide more accurate reconstruction for buried objects with a much less iteration step than those required in the original CSI scheme.

3. Results: Numerical Test

3.1 Numerical Setting

This section describes FDTD-based numerical tests, where a three-multilayer model is assumed. The 17 sets of transmitter and receiver are linearly arranged along $y = 200$ mm with 100 mm spacing. The raised cosine modulated pulse with a center frequency of 0.5 GHz and a bandwidth of 0.4 GHz is set assuming the L-band GPR scenario. Tables 1 and 2 show the dimensions of each layer or object and the dielectric parameters for the two different GPR models, where the buried object is assumed to be an air cavity. These parameters were extracted from the literature [12], assuming dry or wet sand or clay. In particular, Case 1 assumes sand dry media for all layers, and Case 2 presents the sandy dry soil for the 1st layer, sandy wet soil for the 2nd layer, and a clay saturated layer. The cell sizes for both FDTD and CSI are set to 10 mm, and the total number of cell sizes allocated to all multilayer regions is 9600, whereas the number of data samples is 289, which means a much more severe ill-posed case. A Gaussian white noise is added to the scattered electric field in the time domain, and the signal-to-noise ratio (SNR) is defined as the time domain ratio of maximum

Table 1 Dimensions of each layer and object.

Object	Dimension [mm]
Back ground medium	2000×1000
Layer 1	1600×200
Layer 2	1600×200
Layer 3	1600×200
Buried Object	100×100

Table 2 Dielectric property for each model.

Object	#1		#2	
	ϵ_r	σ[S/m]	ϵ_r	σ[S/m]
Back ground medium	1	0	1	0
Layer 1	4	1.00×10^{-7}	5	1.00×10^{-3}
Layer 2	5	1.00×10^{-4}	15	1.00×10^{-2}
Layer 3	6	1.00×10^{-3}	35	1.00×10^{-1}
Buried Object	1	0	1	0

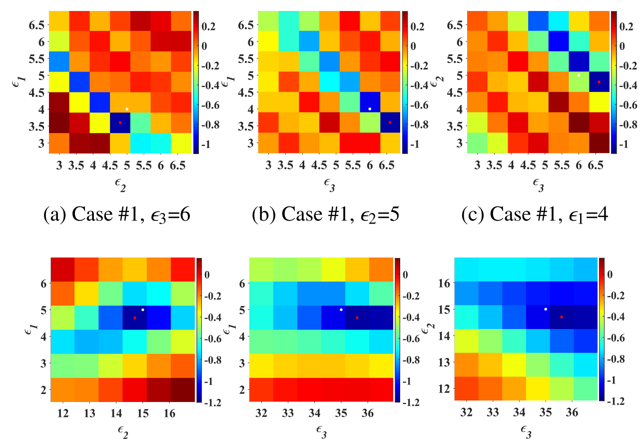

(a) Case #1, ϵ_3=6 (b) Case #1, ϵ_2=5 (c) Case #1, ϵ_1=4

(d) Case #2, ϵ_3=35 (e) Case #2, ϵ_2=15 (f) Case #2, ϵ_1=5

Fig. 4 Cross-sectional profiles of residuals of the cost function in each case at the case of SNR of 20 dB. White and red dots are true and estimated permittivity, respectively.

Table 3 Estimation results for relative permittivity at the case of SNR of 20 dB.

Model	Relative permittivity					
	Layer 1		Layer 2		Layer 3	
	True	Est.	True	Est.	True	Est.
#1	4	3.90	5	5.01	6	6.10
#2	5	5.45	15	16.1	35	31.6

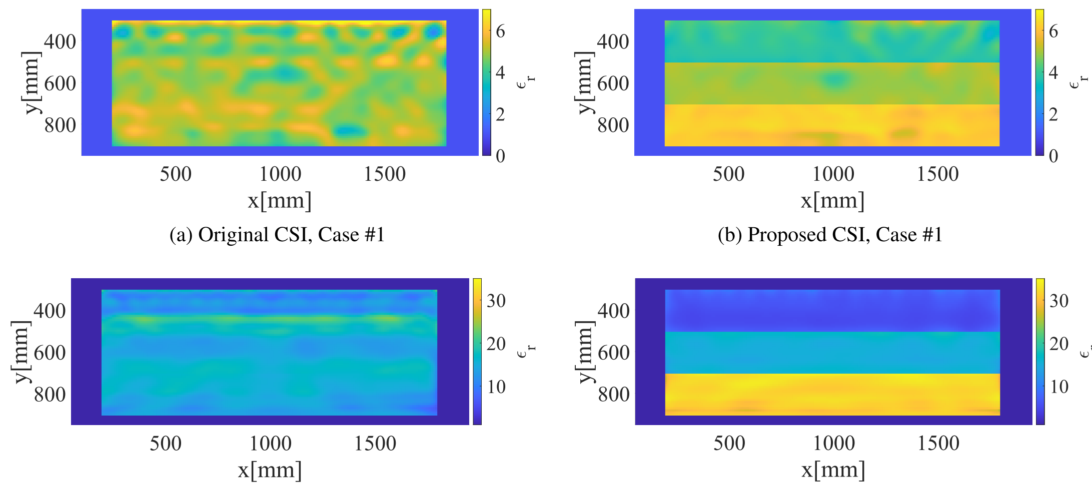

(a) Original CSI, Case #1 (b) Proposed CSI, Case #1

(c) Original CSI, Case #2 (d) Proposed CSI, Case #2

Fig. 5 Reconstruction results in each case at the SNR of 20 dB. Color denotes the relative permittivity.

signal power to the noise variance. In this case, considering the same practical scenario as in [13], 20 dB SNR is assumed.

3.2 Permittivity Estimation for Multiple Layer

This section first introduces the results for permittivity estimation by the proposed method, namely, the process from Eq. (6) to Eq. (9). Note that, the total field in the ROI is given by the FDTD to focus on the validation of the proposed scheme. Figure 4 shows each cross-sectional profile for the minimized residual of the CSI cost function, namely, $\tilde{F}(\boldsymbol{\epsilon}_{\rm ML})$ for each combination of $\boldsymbol{\epsilon}_{\rm ML}$. In Case #1 and #2, 7 and 6 different samples for permittivity in each layer are investigated, respectively, at the optimization process in Eqs. (7) and (9). This figure shows that the proposed scheme accurately determines each relative permittivity, using the minimized cost function in each case. Table 3 shows the permittivity estimation results for each case, where more densely sampled search in Eq. (8) is sequentially done from the results in Fig. 4. This table shows that our proposed method retains high accuracy for each layer's permittivity estimation in each case. Note that the reconstruction accuracy for the third layer Case #2 is relatively worse than that in Case #1. This is because each layer in Case #2 has relatively larger conductivity, and the reflection responses from the second and third layer would be considerably smaller than those in Case #1.

3.3 Reconstruction for Buried Objects

Figure 5 shows the reconstruction images obtained by the original and proposed CSI methods for Cases # 1 and # 2, respectively. Here, the original CSI method is calculated from an initial estimate of permittivity of the 2nd layer media. The original CSI method could not provide both the object profile and the permittivities for the three layers' background media because of the inappropriate initial estimate and highly ill-conditioned scenario. However, the proposed method could provide a dielectric profile for buried objects using a suitable initial estimate of background media, which alleviates the local optimal issue in such an ill-conditioned problem. Table 4 shows the root mean square errors for relative permittivity estimations, which also verifies the proposed method's effectiveness. Note that, in Case # 2, the dielectric profile for buried object (air) would not be clearly reconstructed, compared with that in Case #1. This is because the dielectric contrast between air and background media is much higher in Case #2, and it leads the difficulty to reach the global optimum solution. A more suitable initial estimate would be a promising solution for this problem, and this is our future task.

Table 4 RMSE of relative permittivity at the case of SNR of 20 dB.

Case	Original CSI	Proposed method
#1	0.99	0.42
#2	13.35	2.67

4. Conclusion

This study introduced a CSI-based dielectric profile reconstruction assuming a multiple layer ground model for a microwave subsurface imaging scenario. To begin, by substantially reducing the number of unknowns using a homogeneous assumption, the relative permittivity estimation scheme provides an accurate estimate for each layer's permittivity by minimizing the CSI cost function. Subsequently, a post-CSI approach reconstructs a buried object profile using an appropriate initial estimate of multilayered background media. The 2D FDTD numerical analysis demonstrated that our proposed scheme would work much better than that obtained by the original CSI method and could recognize an air cavity object in a high-contrast multilayered medium. We are now working on experimental and 3D investigations.

Acknowledgments

This research was supported by JST FOREST Program, Grant Number JPMJFR2025, Japan.

References

[1] C. Özdemir, Ş. Demirci, E. Yiğit, and B. Yilmaz, “A Review on Migration Methods in B-Scan Ground Penetrating Radar Imaging,” Mathematical Problems in Engineering., vol.2014, 280738, pp.1–16, 2014.
[2] N. Smitha, D.R.U. Bharadwaj, S. Abilash, S.N. Sridhara, and V. Singh, “Kirchhoff and F-K migration to focus ground penetrating radar images,” Geo-Engineering, vol.7, no.4, 2016.
[3] E. Pettinelli, A.D. Matteo, E. Mattei, L. Crocco, F. Soldovieri, J.D. Redman, and A.P. Annan, “GPR Response From Buried Pipes: Measurement on Field Site and Tomographic Reconstructions,” IEEE Trans. Geosci. Remote Sens., vol.47, no.8, pp.2639–2645, Aug. 2009.
[4] M. González-Díaz, M. García-Fernández, Y. Álvarez-López, and F. Las-Heras, “Improvement of GPR SAR-Based Techniques for Accurate Detection and Imaging of Buried Objects,” IEEE Trans. Instrum. Meas., vol.69, no.6, pp.3126–3138, June 2020.
[5] W. Zhang and A. Hoorfar, “MIMO Ground Penetrating Radar Imaging Through Multilayered Subsurface Using Total Variation Minimization,” IEEE Trans. Geosci. & Remote Sens., vol.57, no.4, pp.2107–2115, April 2019.
[6] F. Soldovieri, J. Hugenschmidt, R. Persico, and G. Leone, “A linear inverse scattering algorithm for realistic GPR applications,” Near Surface Geophysics, vol.5, no.1, pp.29–41, Feb. 2007.
[7] C.-P. Kao, J. Li, Y. Wang, H. Xing, and C.R. Liu, “Measurement of Layer Thickness and Permittivity Using a New Multilayer Model From GPR Data,” IEEE Trans. Geosci. Remote Sens., vol.45, no.8, pp.2463–2470, Aug. 2007
[8] P.M. van den Berg and R.E. Kleinman, “A contrast source inversion method,” Inv. Probl., vol.13, no.6, pp.1607–1620, July 1997.
[9] P.M. van den Berg, A. Abubakar, N.V. Budko, and R.F. Remis, “Imaging and Inversion of Buried Objects using GPR,” IGARSS 2001. Scanning the Present and Resolving the Future. Proceedings. IEEE 2001 International Geoscience and Remote Sensing Symposium (Cat. No.01CH37217), vol.3, pp.1377–1380, July 2001.
[10] H. Morimoto, Y. Yamauchi, and S. Kidera, “Contrast Source Inversion-Based Multilayered Object Analysis for Terahertz Wave Imaging,” IEEE Geosci. & Remote Sensing Letters, vol.19, pp.1–5, 2022.
[11] Y. Yamaucnhi and S. Kidera, “Contrast Source Inversion Based Object Reconstruction Buried in Multi-layered Background for Microwave Subsurface Imaging,” 2021 IEEE USNC-URSI Radio Science Meeting (Joint with AP-S Symposium), pp.74–75, 2021.
[12] J.B. Rhebergen, H.A. Lensen, P.B.W. Schwering, G.R. Marin, and J.M.H. Hendrickx, “Soil moisture distribution around land mines and the effect on relative permittivity,” Proceedings of SPIE, vol.4742, pp.269–280, Aug. 2002
[13] S. Takahashi and S. Kidera, “Acceleration of Range Points Migration Based Microwave Imaging for Non-destructive Testing,” IEEE Antenna Wireless Propagation Letters, vol.17, no.4, pp.702–705, April 2018.